Technical Report
DL-TR-01-001
May 2001

Numerical Simulation of Low Reynolds Number Slip Flow Past a Confined Microsphere

R. W. Barber and D. R. Emerson

Centre for Microfluidics,
Department of Computational Science and Engineering,
CLRC Daresbury Laboratory,
Daresbury,
Warrington,
WA4 4AD.

Abstract

One of the major difficulties in simulating gas transport through micron-sized devices is caused by the fact that the continuum flow hypothesis implemented in the Navier-Stokes equations begins to break down when the dimensions of the flow domain are comparable to the mean free path of the molecules. Under such conditions the fluid can no longer be regarded as being in thermodynamic equilibrium and a variety of non-continuum or rarefaction effects are likely to be exhibited. Velocity profiles, boundary wall shear stresses, mass flow rates and hydrodynamic drag forces are all affected by the non-continuum regime and consequently microfluidic devices which are simply scaled down versions of macro-scale systems may not always function as intended.

This study investigates the important problem of low Reynolds number rarefied gas flow past a confined microsphere within a circular pipe. The geometry of a confined sphere is utilised in conventional spinning-rotor vacuum gauges where the drag on an electro-magnetically suspended rotating sphere can be used to measure a number of important physical properties of a rarefied gas including pressure, viscosity or molecular weight. Similar principles have been envisaged for the measurement of flow rates and pressures in microfluidic devices.

In the present investigation, the problem has been restricted to the estimation of the drag forces on a stationary (non-rotating) sphere. Numerical simulations are carried out over a range of Knudsen numbers covering the continuum and slip flow regimes ($0 \le Kn \le 0.1$). In addition, blockage effects are studied by varying the ratio between the diameter of the pipe and the diameter of the sphere, H / D. The results indicate that blockage effects are extremely important in the continuum flow regime and cause an amplification in the drag force on the sphere. However, blockage phenomena are found to be less significant as the Knudsen number is increased. At the upper limit of the slip flow regime ($Kn \simeq 0.1$), blockage amplification is shown to be reduced by almost 50% for a pipe-sphere geometry of $H / D = 2$.

Contents

1 Introduction

In recent years, rapid progress in micro-fabrication and assembly techniques has led to the development of extremely small-scale machines commonly referred to as MEMS - Micro-Electro-Mechanical Systems [1]. MEMS are generally defined as electro-mechanical devices having a characteristic length scale between 1 mm and 1 μm. Actuators employing electrostatic, magnetic, pneumatic or thermal control techniques have recently been constructed down to 100 μm in size [2] whilst motors and gear wheels have also been demonstrated at similar scales [3]. In addition, miniaturised sensors are already commercially available for the measurement of parameters such as temperature, pressure, angular velocity and acceleration.

An increasing number of MEMS applications involve the manipulation of one or more fluids [4,5]. Examples include miniaturised heat-exchanges to cool integrated circuits [6], micro-reactors to generate small quantities of dangerous or expensive chemicals [7], "lab-on-a-chip" bio-chemical sensors which perform complex biological assays on sub-nanolitre samples [8], DNA sequencing systems which carry out parallel assays to provide high throughput screening [9] and hand-held gas chromatography systems for the detection of trace concentrations of air-borne pollutants [10]. In addition, the availability of inexpensive arrays of microsensors and microactuators on a robust silicon wafer could eventually lead to the possible use of MEMS devices for flow control and drag reduction on submarines and ships [11]. A common link between all these examples is the requirement to move fluid through or over the device in a controlled manner. However, one of the emerging issues in MEMS research is the realisation that the fluid mechanics at such small scales is not necessarily the same as that experienced in the macroscopic world.

Surface effects will obviously dominate the flow regime in microfluidic systems. For example, the surface-to-volume ratio for a device with a characteristic length of 1 m is 1 m^{-1} whilst the surface-to-volume ratio for a MEMS device having a characteristic length of 1 μm will increase to 10^6 m^{-1}. This million-fold increase in the surface area relative to the volume will dramatically affect the transfer of mass, momentum and energy through the device. Inertial forces will be small whilst surface friction and viscous effects will dominate the fluid motion. The small length scales of micro-devices may also invalidate the continuum flow hypothesis employed in conventional fluid mechanics. As a consequence, microfluidic systems which are simply scaled down versions of macro-scale devices may not always function as intended.

Experiments conducted by Pfahler *et al.* [12], Harley *et al.* [13] and Arkilic *et al.* [14-17] on the flow of gases and liquids in silicon micro-machined channels indicate that conventional analyses are unable to predict flow rates in micron-sized devices with any degree of accuracy. Pfahler *et al.* [12] found that the observed pressure drop along a microchannel was lower than expected, signifying the breakdown of the continuum flow hypothesis. In the case of liquids they postulated that the viscosity at very small scales might be lower than the conventional viscosity coefficient employed in macroscopic analyses.

Until recently, non-continuum gas flows were only encountered in specialised low-density applications such as high-altitude aircraft or high-vacuum equipment.

However, the small lengths scales commonly encountered in microfluidic devices imply that rarefaction effects will influence the flow characteristics at atmospheric pressure. As a consequence, the continuum hypothesis of the Navier-Stokes equations cannot be justified and more elaborate analysis techniques are required to predict gas transport within miniaturised devices.

For an ideal gas modelled as rigid spheres, the mean free path of the molecules, $\mathcal{L}$, can be related to the temperature, T, and pressure, p, via the following equation [18]:

$$\mathcal{L} = \frac{kT}{\sqrt{2}\,\pi\, p\, \sigma_c^2} \tag{1}$$

where

k = Boltzmann's constant $= 1.380662 \times 10^{-23}$ J / K,

T = temperature (K),

p = pressure (N/m^2) and

σ_c = collision diameter of the molecules (m).

The continuum flow hypothesis is valid provided the mean free path of the molecules is smaller than the characteristic dimensions of the flow domain. If this condition is violated, the fluid will no longer be under local thermodynamic equilibrium and the linear relationship between the shear stress and rate of shear strain (Newton's law of viscosity) cannot be applied. Velocity profiles, boundary wall shear stresses, mass flow rates and pressure differences will all be influenced by non-continuum effects. In addition, the conventional no-slip boundary condition imposed at a solid-fluid interface will begin to break down even before the linear stress-strain relationship becomes invalid (Gad-el-Hak [5]).

The ratio between the mean free path, $\mathcal{L}$, and the characteristic length of the flow geometry, L, is commonly referred to as the Knudsen number:

$$Kn = \frac{\mathcal{L}}{L} \tag{2}$$

Essentially the value of the Knudsen number, Kn, determines the degree of rarefaction of the gas and the validity of the continuum hypothesis. Schaaf & Chambre [19] have proposed the following classification system for the flow regime based upon the local Knudsen number: For $Kn \le 10^{-2}$, the continuum hypothesis is appropriate and the Navier-Stokes equations can be employed using conventional no-slip boundary conditions. Conversely, for $Kn \ge 10$, the continuum approach breaks down completely and the regime can then be described as being a *free molecular flow*. Under such conditions, the mean free path of the molecules is far greater than the characteristic length scale and consequently molecules reflected from a solid surface travel, on average, many lengths scales before colliding with other molecules. It is thus valid to neglect the effect of the reflected particles on the incident flow stream, and treat the incident and reflected molecular flows separately (Schaaf & Chambre [19]). However, for Knudsen numbers between $Kn = 10^{-2}$ and $Kn = 10$, the

fluid can neither be considered an absolutely continuous medium nor a free molecular flow. A further sub-classification is therefore necessary to distinguish between the appropriate method of analysis. For $10^{-2} \le Kn \le 10^{-1}$ (commonly referred to as the *slip flow* regime), the Navier-Stokes equations can be used provided appropriate slip-velocity conditions are implemented along the walls. On the other hand, for $10^{-1} \le Kn \le 10$ (*transition flow*), the continuum assumption of the Navier-Stokes equations begins to break down and alternative methods of simulation such as particle based DSMC (Direct Simulation Monte Carlo) approaches must be employed (Bird [20]).

As an example of Schaaf & Chambre's flow classification system, consider a microfluidic device transporting air inside a $1\,\mu m$ channel at SATP - standard ambient temperature and pressure (T = 298.15 K and $p = 10^5$ N/m^2). The average collision diameter of the air molecules is approximately 3.66×10^{-10} m (Appendix A), giving a mean free path from eqn. (1) of $\mathcal{L} = 0.0692\,\mu m$. A microchannel with a characteristic height of $1\,\mu m$ would have a Knudsen number of $Kn = 0.0692$ (which is within the slip flow regime) and therefore the Navier-Stokes equations can be used in the analysis provided slip-velocity boundary conditions are implemented along the solid walls. On the other hand, if the pressure in the same microfluidic device were lowered to 0.1 atmospheres, the Knudsen number would increase to $Kn = 0.692$ (the transition regime) and the Navier-Stokes equations would no longer be valid. As an aside, it should be noted that the mean free path of a gas is inversely proportional to the square of the molecular collision diameter, σ_c, and therefore light gases such as hydrogen or helium have longer mean free paths and consequently increased Knudsen numbers compared to air (Gad-el-Hak [5]).

The present study investigates low Reynolds number (laminar) slip flow past a confined microsphere inside a circular pipe, as illustrated schematically in Figure 1. The geometry of a sphere inside a circular pipe is commonly utilised in macro-scale spinning-rotor vacuum gauges as described by Fremerey [21,22] and Reich [23]. Essentially, the rate of damping of an electro-magnetically suspended rotating sphere can be used to measure a number of important properties of a rarefied gas including pressure, viscosity and molecular weight. In the context of MEMS applications, a microsphere inside a fine-bore capillary tube could be employed as a miniaturised spinning-rotor device to provide accurate measurement of the flow rate. Alternatively, a microsphere located axisymmetrically within a circular cone could be used as a microvalve to control the flow. Adjusting the position of the sphere along the axis of the cone allows the blockage ratio to be altered thereby controlling the pressure difference across the device. Confined microspheres have also been utilised in continuous-flow cells to provide efficient turbulent mixing of liquid reagents for monitoring reactions with micro-second time-scales (Shastry *et al*. [24]). Although this final application occurs in a totally different flow regime, it serves to illustrate the practical importance of such a simple geometry.

Low Reynolds number rarefied gas flows past a confined microsphere have been studied numerically by Liu *et al.* [25] over a wide range of Knudsen numbers covering the continuum, slip and transitional flow regimes. Liu *et al*. also investigated blockage effects by varying the ratio between the diameter of the pipe and the diameter of the sphere (H / D). The present investigation aims to provide an

independent re-assessment of the drag forces experienced by a confined microsphere in the continuum ($Kn \to 0$) and slip flow ($Kn \le 10^{-1}$) regimes. A preliminary validation exercise is conducted in the continuum flow regime by comparing the computed drag force against analytical solutions for low Reynolds number flow past a confined sphere [26-30]. The numerical model is then used to compute the drag force components in the slip flow regime. Wherever possible, the numerical model is validated against theoretical solutions to confirm the accuracy of the predictions.

2 Governing hydrodynamic equations

The equations governing the flow of a continuous (infinitely divisible) fluid can be written in tensor notation as follows:

continuity:

$$\frac{\partial \rho}{\partial t} + \frac{\partial (\rho u_k)}{\partial x_k} = 0 \tag{3}$$

momentum:

$$\frac{\partial (\rho u_i)}{\partial t} + \frac{\partial (\rho u_k u_i)}{\partial x_k} = -\frac{\partial p}{\partial x_i} + \frac{\partial \tau_{ik}}{\partial x_k} \tag{4}$$

where u is the velocity, p is the pressure, ρ is the fluid density and τ_{ik} is the second-order stress tensor. For a Newtonian, isotropic fluid, the stress tensor is given by

$$\tau_{ik} = \mu \left(\frac{\partial u_i}{\partial x_k} + \frac{\partial u_k}{\partial x_i} \right) + \lambda \left(\frac{\partial u_j}{\partial x_j} \right) \delta_{ik} \tag{5}$$

where μ and λ are the first and second coefficients of viscosity and δ_{ik} is the unit second-order tensor (Kronecker delta). Implementing Stokes' continuum hypothesis [31] allows the first and second coefficients of viscosity to be related via

$$\lambda + \frac{2}{3}\mu = 0 \tag{6}$$

although the validity of the above equation has occasionally been called into question for fluids other than dilute monatomic gases (Gad-el-Hak [32]). Assuming Stokes' hypothesis is valid allows the viscous stress tensor to be rewritten in the more familiar form:

$$\tau_{ik} = \mu \left(\frac{\partial u_i}{\partial x_k} + \frac{\partial u_k}{\partial x_i} \right) - \frac{2}{3}\mu \left(\frac{\partial u_j}{\partial x_j} \right) \delta_{ik} \tag{7}$$

For a two-dimensional axisymmetric flow in a cylindrical co-ordinate system, the governing Navier-Stokes equations can thus be expressed as

continuity:

$$\frac{\partial \rho}{\partial t}+\frac{\partial(\rho u)}{\partial x}+\frac{1}{r}\frac{\partial(\rho r v)}{\partial r}=0 \tag{8}$$

x-momentum:

$$\begin{aligned}\frac{\partial(\rho u)}{\partial t}+\frac{\partial(\rho u u)}{\partial x}+\frac{1}{r}\frac{\partial(\rho r u v)}{\partial r}-\frac{\partial}{\partial x}\left(\mu\frac{\partial u}{\partial x}\right)-\frac{1}{r}\frac{\partial}{\partial r}\left(r\mu\frac{\partial u}{\partial r}\right)=\\ -\frac{\partial}{\partial x}\left(p+\frac{2}{3}\mu\nabla.\mathbf{V}\right)+\frac{\partial}{\partial x}\left(\mu\frac{\partial u}{\partial x}\right)+\frac{1}{r}\frac{\partial}{\partial r}\left(r\mu\frac{\partial v}{\partial x}\right)\end{aligned} \tag{9}$$

r-momentum:

$$\begin{aligned}\frac{\partial(\rho v)}{\partial t}+\frac{\partial(\rho u v)}{\partial x}+\frac{1}{r}\frac{\partial(\rho r v v)}{\partial r}-\frac{\partial}{\partial x}\left(\mu\frac{\partial v}{\partial x}\right)-\frac{1}{r}\frac{\partial}{\partial r}\left(r\mu\frac{\partial v}{\partial r}\right)=\\ -\frac{\partial}{\partial r}\left(p+\frac{2}{3}\mu\nabla.\mathbf{V}\right)+\frac{\partial}{\partial x}\left(\mu\frac{\partial u}{\partial r}\right)+\frac{1}{r}\frac{\partial}{\partial r}\left(r\mu\frac{\partial v}{\partial r}\right)-\frac{2\mu v}{r^2}\end{aligned} \tag{10}$$

where u is the velocity component in the x-direction and v is the velocity component in the r-direction. The divergence of the velocity field, $\nabla.\mathbf{V}$, in cylindrical co-ordinates is given by

$$\nabla.\mathbf{V}=\frac{\partial u}{\partial x}+\frac{1}{r}\frac{\partial(r v)}{\partial r} \tag{11}$$

3 Slip-velocity boundary conditions

In traditional (continuum) flow analyses, a no-slip velocity constraint is enforced along all solid-fluid interfaces. The notion behind the no-slip condition arises from the fact that there should be no discontinuities in the velocity field within the fluid as this would give rise to infinite velocity gradients and therefore infinite shear stresses (Gad-el-Hak [5]). A similar argument can be employed for conditions at the wall and therefore discontinuities in velocity are also not allowed at the solid-fluid interface. However, the no-slip constraint is strictly only valid if the fluid adjacent to the surface is in local thermodynamic equilibrium; a condition which requires a very high frequency of molecular collisions with the wall. In practice, the no-slip condition is found to be appropriate provided the Knudsen number, $Kn<10^{-2}$. If the Knudsen number is increased beyond this value, rarefaction effects start to influence the flow and the molecular collision frequency per unit area becomes too small to ensure thermodynamic equilibrium. Under such conditions, a discontinuity in the tangential velocity will form at any solid-fluid interface.

To account for non-continuum (rarefaction) effects, the Navier-Stokes equations are solved in conjunction with the slip-velocity boundary condition first proposed by Basset [33]:

$$\tau_t = \beta u_t \tag{12}$$

where u_t is the tangential slip-velocity at the wall, τ_t is the tangential shear stress on the wall and β is the slip coefficient. Schaaf & Chambre [19] have shown that the slip coefficient, β, can be related to the mean free path of the molecules as follows:

$$\beta = \frac{\mu}{\left(\frac{2-\sigma}{\sigma}\right)\mathcal{L}} \tag{13}$$

where μ is the viscosity of the gas, σ is the tangential momentum accommodation coefficient (TMAC) and $\mathcal{L}$ is the mean free path. The tangential momentum accommodation coefficient is introduced into the equation to account for the reduction in the momentum of molecules colliding with the wall (Schaaf & Chambre [19]). For an idealised wall (perfectly smooth at the molecular level), the angles of incidence and reflection of molecules colliding with the wall are identical and therefore the molecules conserve their tangential momentum. This is referred to as *specular reflection* and results in perfect slip at the boundary. Conversely, in the case of an extremely rough wall, the molecules are reflected at a totally random angle and lose, on average, their entire tangential momentum: a situation referred to as *diffusive reflection*. In the case of real walls, some molecules will reflect diffusively and some will reflect specularly, and therefore the tangential momentum accommodation coefficient, σ, is used to define the proportion of molecules reflected diffusively. As well as being dependent upon the surface finish of the wall, the value of σ is influenced by the particular solid and gas involved (Arkilic *et al.* [34]).

Equations (12) and (13) can be combined and rearranged to give

$$u_t = \frac{2-\sigma}{\sigma}\frac{\mathcal{L}}{\mu}\tau_t \tag{14}$$

It is convenient at this stage to recast the mean free path in eqn. (14) in terms of the non-dimensionalised Knudsen number, *Kn*. The choice of the characteristic length scale used in the definition of the Knudsen number depends crucially upon the flow geometry under consideration. In the case of flow past a confined microsphere within a circular pipe, Liu *et al.* [25] chose to utilise the diameter of the sphere as the appropriate length scale. Thus, the Knudsen number, *Kn*, is defined as the ratio of the mean free path of the molecules, $\mathcal{L}$, to the diameter of the sphere, *D*:

$$Kn = \frac{\mathcal{L}}{D} \tag{15}$$

Consequently, eqn. (14) can be recast as

$$u_t = \frac{2-\sigma}{\sigma}\frac{Kn\,D}{\mu}\tau_t \tag{16}$$

The governing hydrodynamic equations were solved using THOR-2D – a two-dimensional finite-volume Navier-Stokes solver developed by the Computational Engineering Group at CLRC Daresbury Laboratory (Gu & Emerson [35]). As the flows investigated in the study had relatively low Mach numbers, compressibility effects were ignored and the fluid was considered to be incompressible. Additional subroutines were developed to account for the tangential slip-velocity at the walls of the flow domain (eqn. 16). Since the governing hydrodynamic equations were solved using a non-orthogonal boundary-fitted co-ordinate system, the tangential shear stress at the solid-fluid interface had to be evaluated using a generalised stress tensor transformation procedure, as described in Appendix B. Transforming the stress tensor into a localised co-ordinate reference frame based upon the orientation of the boundary surface provides the hydrodynamic code with greater flexibility for future studies.

4 Boundary conditions

The imposed boundary conditions for the confined microsphere geometry are detailed schematically in Figure 2. It should be noted that the problem has been non-dimensionalised and therefore the mean velocity at the entrance to the pipe, $\overline{u}$, the density of the fluid, ρ, and the diameter of the microsphere, D, are defined as unity. With reference to Figure 2, the boundary conditions are specified as follows:

(a) ***Inflow boundary****:*
The velocity distribution at the pipe entrance can be specified in one of two ways: either the velocity can be assumed uniform across the entrance or alternatively a fully-developed parabolic slip-velocity profile can be prescribed to simulate an infinitely long pipe upstream of the computational domain. In the case of a uniform velocity distribution, the boundary conditions are simply defined as

$$u = 1 \quad \text{and} \quad v = 0 \qquad \text{at} \qquad x = -l \;,\; 0 \le \mathrm{r} \le \frac{H}{2} \tag{17}$$

where H is the diameter of the pipe and l is the longitudinal distance between the inflow boundary and the centre of the sphere.

Alternatively, a fully-developed slip-velocity profile can readily be obtained from the axial-direction Navier-Stokes equation (as detailed by Barber & Emerson [36]). It can be shown that the theoretical velocity profile across the pipe is given by

$$u(r) = 2\overline{u}\,\frac{\left(1 - \dfrac{r^2}{R^2} + 4\,\dfrac{2-\sigma}{\sigma}\,Kn_p\right)}{\left(1 + 8\,\dfrac{2-\sigma}{\sigma}\,Kn_p\right)} \tag{18}$$

where $\overline{u}$ is the mean velocity, R is the radius of the pipe and Kn_p is the Knudsen number based upon the pipe diameter, i.e.

$$Kn_p = \frac{\mathcal{L}}{H} \tag{19}$$

Comparison of the Knudsen number definitions presented in eqns. (15) & (19) reveals

$$\frac{Kn_p}{Kn} = \frac{D}{H} \qquad \text{or} \qquad Kn_p = \frac{Kn}{H/D} \tag{20}$$

Employing the fact that $R = H/2$ and using the result shown in eqn. (20) enables the velocity distribution across the pipe to be recast in terms of the localised Knudsen number on the sphere, *Kn*, and the blockage ratio, H/D:

$$u(r) = 2\overline{u}\,\frac{\left(1 - \frac{4r^2}{H^2} + 4\,\frac{2-\sigma}{\sigma}\,\frac{Kn}{H/D}\right)}{\left(1 + 8\,\frac{2-\sigma}{\sigma}\,\frac{Kn}{H/D}\right)} \tag{21}$$

As an aside, in the limit of $Kn \to 0$ (i.e. the continuum flow solution), eqn. (21) reverts to the familiar no-slip (NS) velocity profile given by Hagen-Poiseuille pipe theory (see Schlichting [37]) :

$$u_{\mathrm{NS}}(r) = 2\overline{u}\left(1 - \frac{4r^2}{H^2}\right) \tag{22}$$

The slip-velocity inflow boundary condition can thus be formally defined as

$$u(r) = 2\overline{u}\,\frac{\left(1 - \frac{4r^2}{H^2} + 4\,\frac{2-\sigma}{\sigma}\,\frac{Kn}{H/D}\right)}{\left(1 + 8\,\frac{2-\sigma}{\sigma}\,\frac{Kn}{H/D}\right)} \text{ and } v(r) = 0 \quad \text{at} \quad x = -l \;,\; 0 \le \mathrm{r} \le \frac{H}{2} \tag{23}$$

Comparison of the drag experienced by the sphere for the uniform and fully-developed entrance velocity profiles can be used to assess whether a particular hydrodynamic mesh has sufficient length to ensure the flow around the sphere is independent of the imposed upstream boundary condition.

(b) ***Pipe wall boundary****:*

The tangential slip-velocity along the wall of the pipe is evaluated using eqn. (16) as detailed in Section 3. In addition, there must be zero normal flow across the wall. By definition, the pipe is aligned with the *x*-direction, and therefore the boundary conditions are specified as follows:

$$u = \frac{2-\sigma}{\sigma}\,\frac{Kn\,D}{\mu}\,\tau_t \quad \text{and} \quad v = 0 \qquad \text{at} \qquad r = \frac{H}{2} \;,\; -l \le x \le l \tag{24}$$

where $2l$ is the total length of the flow domain and τ_t is the tangential shear stress on

the wall, evaluated using the stress tensor transformation procedure described in Appendix B.

(c) ***Centreline boundary****:*
The flow must be symmetrical about the centreline of the pipe. Hence,

$$\frac{\partial u}{\partial r} = 0 \quad \text{and} \quad v = 0 \qquad \text{at} \qquad r = 0 \ , \ \begin{cases} -l \le x \le -a \\ a \ge x \ge l \end{cases} \tag{25}$$

where a is the radius of the microsphere.

(d) ***Outflow boundary****:*
The flow will approach fully-developed conditions at the downstream boundary and consequently the longitudinal gradients of the velocity components should tend to zero, i.e.

$$\frac{\partial u}{\partial x} = 0 \quad \text{and} \quad \frac{\partial v}{\partial x} = 0 \qquad \text{at} \qquad x = l \ , \ 0 \le r \le \frac{H}{2} \tag{26}$$

(e) ***Microsphere wall boundary****:*
The tangential slip-velocity along the wall of the microsphere is evaluated using eqn. (16) as detailed in Section 3. In addition, there must be zero normal flow across the surface. Hence, the boundary conditions can be expressed as

$$u_t = \frac{2-\sigma}{\sigma} \frac{Kn\, D}{\mu} \tau_t \quad \text{and} \quad u_n = 0 \qquad \text{at} \qquad x^2 + r^2 = a^2 \tag{27}$$

where u_t is the tangential slip-velocity and u_n is the normal velocity component on the surface of the sphere. The localised velocity vector (u_t, u_n) is then transformed into the global velocity vector (u, v) by appropriate trigonometric mapping employing the orientation of the unit tangential base vector of the surface.

5 Evaluation of the drag on the microsphere

The total drag on the microsphere is composed of three separate components, namely skin friction drag, normal stress drag and pressure (or form) drag. Each drag component has to be determined by numerically integrating the stress distribution around the circumference of the sphere. For the purposes of describing the numerical integration process, a localised spherical polar co-ordinate reference frame (r, θ, α) is established as shown in Figure 3, with the origin at the centre of the sphere and $\theta = 0$ aligned in the direction of the longitudinal axis of the pipe. The localised r co-ordinate illustrated in Figure 3 should not, however, be confused with the two-dimensional cylindrical (x,r) co-ordinate system employed in the governing hydrodynamic equations.

5.1 Drag due to skin-friction

The tangential shear stress acting on the surface of the sphere, $\tau_{r\theta}$, is found using the generalised stress transformation procedure described in Appendix B. The drag force on the sphere can thus be found by resolving the shear stress in the longitudinal *x*-direction and integrating around the entire surface of the sphere. Specifically,

$$\text{Skin-friction drag} = \iint -\tau_{r\theta}\big|_{r=a} \sin\theta \, dS \tag{28}$$

where *a* is the radius of the microsphere and *dS* denotes an infinitesimal surface element. Consider an elemental surface region subtending angles of $d\theta$ and $d\alpha$, bounded by $\theta = \text{constant}$ and $\alpha = \text{constant}$ lines. The surface area of the element can be shown to be

$$dS = a^2 \sin\theta \, d\alpha \, d\theta \tag{29}$$

and hence the drag on the sphere can be evaluated as

$$\text{Skin-friction drag} = a^2 \int_0^{2\pi} d\alpha \int_0^{\pi} -\tau_{r\theta}\big|_{r=a} \sin^2\theta \, d\theta \tag{30}$$

Integrating with respect to α finally yields

$$\text{Skin-friction drag} = 2\pi a^2 \int_0^{\pi} -\tau_{r\theta}\big|_{r=a} \sin^2\theta \, d\theta \tag{31}$$

In the hydrodynamic code, the definite integral in eqn. (31) is replaced by numerical integration using either Simpson's rule (for equispaced boundary nodes) or the trapezoidal rule (for unequal spacings of grid nodes). Further details of the numerical integration schemes can be found in Press *et al*. [38].

5.2 Drag due to normal stress

For continuum (no-slip) flows, it can be shown that the normal stress on the surface of a sphere must be zero in an incompressible Newtonian fluid (Richardson [39]). More generally, it can be shown that the normal stress component must vanish along any rigid no-slip impermeable boundary. In contrast, the tangential slip-velocity boundary condition employed in the analysis of rarefied gas flows generates a non-zero normal stress component and therefore produces an important additional force on the sphere.

Using an analogous integration procedure to that described in the previous section, yields

$$\text{Normal stress drag} = 2\pi a^2 \int_0^{\pi} \tau_{rr}\big|_{r=a} \sin\theta\cos\theta \, d\theta \tag{32}$$

where $\tau_{rr}\big|_{r=a}$ is the normal stress on the surface of the sphere evaluated using the generalised stress transformation procedure described in Appendix B. Once again, the definite integral in eqn. (32) is replaced by numerical integration around the boundary grid nodes representing the sphere.

5.3 Drag due to pressure distribution

The drag on the microsphere due to the pressure distribution (or form drag) is found using a similar integration procedure to that shown in eqn. (32). Noting that the pressure force on the surface is directed *inwards* towards the centre of the sphere leads to

$$\text{Form drag} = 2\pi a^2 \int_0^{\pi} -p\big|_{r=a} \sin\theta\cos\theta \, d\theta \tag{33}$$

The total drag experienced by the microsphere can then be found by summing the three individual drag components presented in eqns. (31), (32) and (33).

6 Numerical results

The numerical model was used to assess the drag experienced by a confined microsphere exposed to low Reynolds number rarefied gas flows. For compatibility with the numerical simulations presented by Liu *et al*. [25], the Reynolds number was defined using the mean velocity in the pipe, $\bar{u}$, and the radius of the sphere, *a*, as the velocity and length scales, i.e.

$$Re = \frac{\rho \bar{u} \, a}{\mu} \tag{34}$$

whilst the Knudsen number was defined using the diameter of the sphere, *D*, as the characteristic length scale:

$$Kn = \frac{\mathcal{L}}{D} \tag{35}$$

Following Liu *et al*. [25], the simulations considered extremely low Reynolds numbers corresponding to the creeping flow conditions originally analysed by Stokes [40]. The Knudsen number was varied from $Kn = 0$ (continuum flow) to $Kn = 0.1$ (a frequently adopted upper bound for the slip flow regime). Moreover, in the absence of additional information, the tangential momentum accommodation coefficient, σ, was assumed to have a value of unity in all computations.

Blockage effects were studied by varying the ratio between the diameter of the pipe and the diameter of the sphere (H / D). The simulations involved a wide range of blockage ratios from $H / D = 2$ up to $H / D = 40$ as detailed in Table 1. Each computational mesh was constructed using three smaller sub-blocks to account for the

individual boundary conditions upstream, downstream and around the sphere. For each blockage ratio, the locations of the inflow and outflow boundaries were chosen sufficiently far from the sphere so as not to affect the computed drag force. The well known observation that fully-developed flow conditions are established within approximately 0.6 pipe diameters of the entrance when $Re \simeq 0$ (Shah & London [41], Barber & Emerson [36]) was used to provide a preliminary estimate of the required boundary locations. Detailed numerical experiments were then conducted using different mesh lengths to ensure the suitability of the chosen boundary positions.

Table 1 also presents details of the mesh resolutions employed for each blockage ratio. Higher numbers of grid cells in the *r*-direction were deemed necessary for the larger H/D ratios due to the increased size of the computational domains. To achieve a reasonably fine grid resolution in the vicinity of the microsphere, an exponential grid stretching was implemented in the axial-direction both upstream and downstream of the sphere. The exponential stretching was chosen so that the grid aspect ratio ($\Delta x/\Delta r$) did not exceed an upper bound of approximately 25 in any of the hydrodynamic meshes. The computational domains were created using GRIDGEN, a commercial grid generation package for structured and unstructured meshes. Numerical experimentation using a number of different grid generation strategies showed that transfinite interpolation yielded the most suitable co-ordinate structure around the sphere. A selection of the computational meshes are presented in Figure 4.

6.1 Continuum flow regime

The first part of the study investigated the drag experienced by the sphere under low Reynolds number continuum flows ($Re \to 0$, $Kn \to 0$). Unconfined creeping flow past a sphere was first analysed by Stokes [40] who demonstrated that in the absence of inertial forces, the total drag force due to the flow of an unbounded incompressible Newtonian fluid could be written as

$$\text{Total drag} = 6\pi\mu U a \tag{36}$$

where U denotes the uniform velocity distribution infinity far from the sphere. In addition, it can be shown that one-third of the total drag can be attributed to the pressure distribution (form drag) whilst the remaining two-thirds are formed by skin friction. Consequently, eqn. (36) can also be written as

$$\text{Form drag} = 2\pi\mu U a \tag{37}$$

and

$$\text{Skin-friction drag} = 4\pi\mu U a \tag{38}$$

A non-dimensionalised drag coefficient, C_D, can then be evaluated by assuming that the total drag on the sphere is related to the dynamic pressure and the projected

frontal area, as described by Schlichting [37]. Defining,

$$\text{Total drag} = C_D \frac{1}{2} \rho U^2 \pi a^2 \tag{39}$$

allows the drag coefficient on the sphere to be written as

$$C_D = \frac{\text{Total drag}}{\frac{1}{2}\rho U^2 \pi a^2} = \frac{6\pi\mu U a}{\frac{1}{2}\rho U^2 \pi a^2} = \frac{12\mu}{\rho U a} = \frac{12}{Re'} \tag{40}$$

where the Reynolds number, Re', is defined using the velocity of the *unbounded* fluid:

$$Re' = \frac{\rho U a}{\mu} \tag{41}$$

Inspection of eqn. (40) reveals that the drag coefficient for an unconfined sphere can be rearranged to give

$$\frac{C_D Re'}{12} = 1 \tag{42}$$

The present study examines the drag force components and blockage effects on a sphere confined within a circular pipe. Consequently, the initial step is to select a suitable method of normalising the computed drag components. The drag coefficient for a confined sphere can be defined using an analogous procedure to that shown in eqn. (40), with the exception that the dynamic pressure is specified in terms of the *mean* velocity in the pipe, $\bar{u}$:

$$C_D = \frac{\text{Total drag}}{\frac{1}{2}\rho \bar{u}^2 \pi a^2} \tag{43}$$

In addition, it is possible to calculate non-dimensionalised drag coefficients for the individual skin-friction and pressure drag components using a similar technique:

$$C_{D\,(\text{skin-friction})} = \frac{\text{Skin-friction drag}}{\frac{1}{2}\rho \bar{u}^2 \pi a^2} \quad \text{and} \quad C_{D\,(\text{form drag})} = \frac{\text{Form drag}}{\frac{1}{2}\rho \bar{u}^2 \pi a^2} \tag{44}$$

The drag coefficients are then normalised with respect to Stokes' unconfined solution using the procedure suggested by Liu *et al*. [25]. Hence, the normalised drag coefficient for a confined sphere can be written as

$$\frac{C_D Re}{12} = \mathcal{F}(H/D) \tag{45}$$

where $\mathcal{F}(H/D)$ denotes a function of the blockage ratio, H/D. The above equation has obvious similarities with the unconfined solution developed in eqn. (42), with the exception that the product of the drag coefficient and the Reynolds number no longer

collapses to a single coefficient but instead depends upon the blockage ratio of the flow geometry. Moreover, it should be noted that the Reynolds number in eqn. (45) is defined in terms of the cross-sectional average velocity in the pipe, $\overline{u}$, rather than the approach velocity of the unbounded fluid as utilised in Stokes' unconfined solution.

In the initial series of tests, a fully developed no-slip velocity profile (eqn. 22) was prescribed at the inflow boundary to simulate a long pipe upstream of the computational domain. Table 2 presents the normalised drag coefficients for $H/D = 2$, the most confined blockage ratio considered. The simulations employed a range of Reynolds numbers between $Re = 0.5$ and $Re = 0.01$ to provide data throughout the low Reynolds number flow regime. It can be seen that the normalised drag coefficients are almost identical, indicating that the product of the drag coefficient, C_D, and the Reynolds number, *Re*, remains invariant in the Stokes' limit ($Re \to 0$). A second study employing a less confined blockage ratio of $H/D = 10$ confirms that the normalised drag coefficient is again independent of the Reynolds number (Table 3). Consequently, at Stokes' limit, the drag is solely dependent upon the blockage ratio, H/D. As an aside, Table 2 also indicates that the ratio between the pressure drag and the total drag deviates from the theoretical value of one-third as predicted by Stokes' unconfined solution. For a blockage ratio of $H/D = 2$, the drag due to the pressure distribution accounts for approximately 52% of the total force, demonstrating that the sphere is being exposed to strong blockage effects. However, for the less confined study presented in Table 3 $(H/D = 10)$, the form drag accounts for approximately 34% of the total force and is therefore very close to the theoretical ratio of one-third.

Normalised drag results for a range of blockage ratios from $H/D = 2$ up to $H/D = 40$ are presented in Table 4 for a Reynolds number, $Re = 0.125$ (as adopted by Liu *et al*. [25]). The results are also illustrated graphically in Figure 5 as a plot of normalised total drag coefficient against blockage ratio. Figure 5 indicates that blockage effects are strongly felt for $H/D < 10$ with a very large increase in the drag coefficient being observed for $H/D < 5$. The computed drag results presented by Liu *et al*. [25] for $H/D \leq 5$ are superimposed on Figure 5 for comparison purposes. The excellent agreement between the two numerical schemes appears to confirm the validity of the present analysis.

In the limit of $H/D \to \infty$, the normalised drag should converge asymptotically to the value predicted by Stokes' solution. Substituting eqn. (36) for the drag on an unconfined sphere into eqn. (43) defining the drag coefficient yields

$$C_D = \frac{6\pi\mu U a}{\frac{1}{2}\rho \overline{u}^2 \pi a^2} = 12\frac{\mu}{\rho \overline{u} a}\frac{U}{\overline{u}} = \frac{12}{Re}\frac{U}{\overline{u}} \tag{46}$$

and therefore the *normalised* drag coefficient tends to

$$\frac{C_D Re}{12} = \frac{U}{\overline{u}} \tag{47}$$

Moreover, as the blockage ratio is increased, the *average* velocity striking the sphere and contributing to the drag will approach the maximum (centreline) velocity in the pipe, $2\overline{u}$. Consequently, in the limit of $H/D \to \infty$, the fluid velocity impinging on

the sphere, *U*, converges to twice the mean velocity in the pipe, i.e.

$$U \to 2\overline{u} \quad \text{as} \quad H/D \to \infty \tag{48}$$

The normalised drag coefficient will therefore tend to a value of 2 for large blockage ratios, i.e.

$$\frac{C_D Re}{12} \to 2 \quad \text{as} \quad H/D \to \infty \tag{49}$$

Figure 5 clearly demonstrates that the computed drag coefficients agree with the theoretical asymptote derived in eqn. (49).

A further validation of the numerical scheme can be achieved by comparing the computed results against the analytical drag formulae presented by Wakiya [26,27], Bohlin [28] and Haberman & Sayre [29]. Wakiya [26] employed Faxen's [42] method of reflections to calculate the drag force on a sphere centrally located in a circular pipe. Two separate flow conditions were considered in the analysis; namely, a sphere moving with constant velocity along the axis of the pipe (analogous to Faxen's drag correction for sedimentation) and secondly, a stationary sphere subjected to Poiseuille pipe flow. By necessity, Wakiya's analytical solution is only valid in the limit, $Re \to 0$, and also has to assume that the ratio between the radius of the sphere, *a*, and the radius of the pipe, r_0, is "small" since the analysis only considers the first two reflections (Happel & Brenner [30]). Wakiya was able to show that the drag force on a confined moving sphere can be approximated as

$$\text{Total drag} = \frac{6\pi\mu U\, a}{\left(1 - 2.104\frac{a}{r_0} + 2.09\frac{a^3}{r_0^3} - 0.95\frac{a^5}{r_0^5}\right)} \tag{50}$$

whereas the force experienced by a stationary sphere in a Poiseuille flow can be expressed as

$$\text{Total drag} = 6\pi\mu U\, a \frac{\left(1 - \frac{2}{3}\frac{a^2}{r_0^2}\right)}{\left(1 - 2.104\frac{a}{r_0} + 2.09\frac{a^3}{r_0^3} - 1.11\frac{a^5}{r_0^5}\right)} \tag{51}$$

where *U* is the velocity of the moving sphere in eqn. (50) or the maximum fluid velocity at the centre of the pipe in eqn. (51). Using the fact that

$$\frac{a}{r_0} = \frac{D}{H} \tag{52}$$

and noting that the maximum velocity in the pipe is twice the mean velocity, the normalised drag coefficient on a stationary confined sphere can be derived as

$$\frac{C_D Re}{12} = \frac{2\left(1 - \frac{2}{3}\frac{D^2}{H^2}\right)}{\left(1 - 2.104\frac{D}{H} + 2.09\frac{D^3}{H^3} - 1.11\frac{D^5}{H^5}\right)} \tag{53}$$

Higher order schemes have been proposed by Bohlin [28] and Haberman & Sayre [29] to increase the range of application to larger values of a/r_0 although the solutions are still only valid in the Stokes' limit, $Re \to 0$. As reported in Happel & Brenner [30], the most accurate solution currently available appears to be the analytical technique proposed by Haberman & Sayre who investigated axisymmetric flow past a confined sphere using an algebraic stream function method. In the case of a moving sphere, Haberman & Sayre [29] demonstrate that the drag force is given by

$$\text{Total drag} = 6\pi\mu U\, a \frac{\left(1 - 0.75857\frac{a^5}{r_0^5}\right)}{\left(1 - 2.1050\frac{a}{r_0} + 2.0865\frac{a^3}{r_0^3} - 1.7068\frac{a^5}{r_0^5} + 0.72603\frac{a^6}{r_0^6}\right)} \tag{54}$$

whilst for the Poiseuille flow case, they show that

$$\text{Total drag} = 6\pi\mu U\, a \frac{\left(1 - \frac{2}{3}\frac{a^2}{r_0^2} - 0.20217\frac{a^5}{r_0^5}\right)}{\left(1 - 2.1050\frac{a}{r_0} + 2.0865\frac{a^3}{r_0^3} - 1.7068\frac{a^5}{r_0^5} + 0.72603\frac{a^6}{r_0^6}\right)} \tag{55}$$

Converting eqn. (55) into the normalised drag coefficient and replacing a/r_0 by D/H yields:

$$\frac{C_D Re}{12} = \frac{2\left(1 - \frac{2}{3}\frac{D^2}{H^2} - 0.20217\frac{D^5}{H^5}\right)}{\left(1 - 2.1050\frac{D}{H} + 2.0865\frac{D^3}{H^3} - 1.7068\frac{D^5}{H^5} + 0.72603\frac{D^6}{H^6}\right)} \tag{56}$$

The analytical solution of Haberman & Sayre (eqn. 56) is included on Figure 5 for comparison purposes. The excellent agreement between the numerical predictions and the analytical solution over the entire range of blockage ratios indicates that the computational scheme provides an accurate representation of the flow past a confined sphere and demonstrates the accuracy of the numerical drag computations. As an aside, the analytical solution presented by Wakiya (eqn. 53) yields almost identical results for $H/D \geq 2$.

To ensure that the computed drag coefficients presented in Table 4 are independent of the imposed inflow boundary condition, the numerical simulations were repeated using a uniform velocity profile at the inlet (Table 5). The computed

drag coefficients were found to agree closely with the results obtained using the fully-developed velocity profile, demonstrating that the hydrodynamic meshes detailed in Table 1 are sufficiently long to ensure that the flow around the sphere is not affected by the upstream boundary. However, as an aside, it should be noted that applying a uniform velocity boundary condition too close to the sphere drastically reduces the computed drag force. This can be explained by the fact that the approaching flow will have insufficient time to settle to a fully-developed profile before reaching the sphere, creating a lower than normal velocity at the centre of the pipe. To demonstrate this effect, Table 6 presents the results of a series of tests employing a range of deliberately shortened hydrodynamic meshes. In order to enhance the drag reduction effects, the simulations were conducted using the widest blockage ratio, $H/D = 40$. Table 6 demonstrates that the computed normalised drag coefficients are reduced as the length available for flow development is decreased. For the shortened hydrodynamic meshes, it can also be seen that the normalised drag coefficient, $(C_D Re/12)$, falls below the theoretical asymptote of 2 as predicted in eqn. (49), indicating that a careless choice of upstream boundary location may result in misleading estimates of drag coefficient.

6.2 Slip flow regime

The second part of the study investigated the drag experienced by the sphere in the slip flow regime ($Kn \le 0.1$). As discussed earlier in Section 3, non-continuum flow effects were incorporated into the hydrodynamic scheme by introducing a tangential slip-velocity boundary condition along the solid walls of the flow domain. Specifically, the slip-flow constraint can be implemented as follows:

$$u_t = \frac{2-\sigma}{\sigma} \frac{Kn\, D}{\mu} \tau_t \tag{57}$$

where u_t is the tangential slip-velocity, τ_t is the shear stress on the wall and σ is the tangential momentum accommodation coefficient. As described in Section 5, the drag due to the normal stress must be included in the slip flow regime and therefore a third non-dimensionalised drag coefficient has to be introduced using a similar procedure to that presented in eqn. (44):

$$C_{D\,(\text{normal stress})} = \frac{\text{Normal stress drag}}{\frac{1}{2}\rho \bar{u}^2 \pi a^2} \tag{58}$$

The total drag coefficient for the sphere is then found by summing the individual drag coefficients due to skin-friction, normal stress and pressure distribution:

$$C_D = C_{D\,(\text{skin-friction})} + C_{D\,(\text{normal stress})} + C_{D\,(\text{form drag})} \tag{59}$$

Table 7 presents the normalised drag coefficients for the most confined blockage ratio, $H/D = 2$. The simulations were conducted using a Reynolds number of $Re = 0.125$ for compatibility with the continuum flow analysis described in

Section 6.1 whilst the Knudsen number was varied from $Kn = 0$ (continuum flow) up to $Kn = 0.1$ (the upper limit of the slip flow regime). A fully-developed slip-velocity profile (eqn. 23) was prescribed at the inflow boundary to simulate an infinitely long pipe upstream of the computational domain and the fluid was again assumed to be incompressible on account of the low Mach numbers found in most microfluidic devices. Additional numerical simulations accounting for compressibility showed very little difference in the predicted drag on the sphere, justifying the low Mach number simplification.

The results in Table 7 indicate that the total drag on the sphere decreases as the Knudsen number is increased, due to a reduction in skin friction and form drag. However, it can also be seen that the drag due to the normal stress increases with Knudsen number, demonstrating the importance of accounting for this term in the slip flow regime. Inspection of the computed normalised drag coefficients for the continuum flow solution reveals a slight inaccuracy in the predictions since the numerical model fails to predict a normal stress drag component of zero as $Kn \to 0$. This discrepancy is thought to be caused by inadequacies in the mesh close to the sphere, but fortunately the error only accounts for a small percentage of the total drag.

Tables 8 & 9 repeat the slip flow computations for blockage ratios of $H/D = 5$ and $H/D = 40$. The results for the three separate blockage ratios are then compared in Figure 6 by plotting the normalised total drag coefficient against Knudsen number. In all cases, the total drag on the sphere decreases as the Knudsen number is increased but the effect is more pronounced as the blockage ratio is reduced. This indicates that blockage effects are much less important in the slip flow regime than for continuum flows.

The normalised drag results for $H/D = 40$ provide a useful validation of the hydrodynamic code since the numerical results should approach the asymptotic limit of low Reynolds number slip flow past an unconfined sphere. Barber & Emerson [43] have previously described an extension of Stokes' analytical solution for creeping flow past a sphere which takes into account non-continuum effects. The analysis follows the slip flow methodology originally proposed by Basset [33] and provides expressions for the individual drag force components and total drag experienced by a microsphere in an unconfined rarefied flow. Following previous work by Goldberg [44] and Schaaf & Chambre [19], the Knudsen number was defined by Barber & Emerson [43] using the radius of the sphere, *a*, as the characteristic length scale, i.e.

$$Kn_a = \frac{\mathcal{L}}{a} \tag{60}$$

The total drag force on an unconfined sphere in the slip flow regime can be shown to be given by

$$\text{Total drag} = 6\pi\mu U\, a \left(\frac{1 + 2\dfrac{2-\sigma}{\sigma} Kn_a}{1 + 3\dfrac{2-\sigma}{\sigma} Kn_a} \right) \tag{61}$$

where U denotes the uniform velocity distribution infinitely far from the sphere and σ

is the tangential momentum accommodation coefficient. Comparing the Knudsen number definitions in eqns. (60) & (15) reveals that

$$\frac{Kn_a}{Kn} = \frac{D}{a} = 2 \qquad \text{or} \qquad Kn_a = 2\,Kn \tag{62}$$

and consequently the total drag can be rewritten in terms of the Knudsen number based on the diameter of the sphere, *Kn*:

$$\text{Total drag} = 6\pi\mu U\, a \left(\frac{1 + 4\dfrac{2-\sigma}{\sigma} Kn}{1 + 6\dfrac{2-\sigma}{\sigma} Kn} \right) \tag{63}$$

In addition, the individual drag components on the sphere can be shown to be:

$$\text{Skin-friction drag} = 4\pi\mu U\, a \left(\frac{1}{1 + 6\dfrac{2-\sigma}{\sigma} Kn} \right) \tag{64}$$

$$\text{Normal stress drag} = 4\pi\mu U\, a \left(\frac{4\dfrac{2-\sigma}{\sigma} Kn}{1 + 6\dfrac{2-\sigma}{\sigma} Kn} \right) \tag{65}$$

and

$$\text{Form drag} = 2\pi\mu U\, a \left(\frac{1 + 4\dfrac{2-\sigma}{\sigma} Kn}{1 + 6\dfrac{2-\sigma}{\sigma} Kn} \right) \tag{66}$$

Figure 7 illustrates the variation in computed normalised drag components on the sphere as a function of Knudsen number for a blockage ratio of $H / D = 40$. The analytical solutions presented in eqns. (63-66) are superimposed on Figure 7 for comparison purposes. It should be noted than in normalising the analytical results, the unconfined flow equations have to be multiplied by a factor of 2 to account for the fact that the fluid velocity impinging on the sphere, *U*, converges to *twice* the mean velocity in the pipe, i.e.

$$U \to 2\,\overline{u} \quad \text{as} \quad H / D \to \infty \tag{67}$$

Thus the normalised total drag coefficient has a theoretical asymptote:

$$\frac{C_D Re}{12} \rightarrow 2\left(\frac{1+4\dfrac{2-\sigma}{\sigma}Kn}{1+6\dfrac{2-\sigma}{\sigma}Kn}\right) \quad \text{as} \quad H/D \rightarrow \infty \tag{68}$$

Analogous equations can also be derived for the theoretical asymptotes of the individual drag force components.

Figure 7 demonstrates good agreement between the numerical and analytical solutions over the entire slip flow regime. Small discrepancies can be seen in the normal stress drag predictions which in turn affect the total drag. This can be confirmed by noting that the numerical model fails to predict a normal stress drag force of zero in the continuum flow regime ($Kn \rightarrow 0$). Previous numerical studies by Beskok & Karniadakis [45] on rarefied gas flows past circular cylinders confirm the difficulty in obtaining accurate estimates of the normal stress distribution. Nevertheless the general agreement between the predictions and the unconfined analytical solution provides an important validation test in the slip flow regime.

In the present study, the error in the normal stress component appears to decrease as the Knudsen number increases. In addition, the numerical model predicts slightly larger skin-friction and form drag components compared to the unconfined analytical solution but this is to be expected since the microsphere should still be experiencing a slight blockage effect due to the pipe walls. The agreement between the numerical and analytical drag components appears to improve as the Knudsen number is increased which again leads to the conclusion that blockage effects becomes less important at higher Knudsen numbers.

Normalised drag results for a range of blockage ratios are presented in Table 10 for a Knudsen number of $Kn = 0.1$ (the upper limit of the slip flow regime). The results are also illustrated graphically in Figure 8 as a plot of normalised total drag coefficient against blockage ratio. Although a general analytical solution for the drag on a confined sphere in the slip flow regime is not presently available, the numerical results can be checked to ensure that the normalised drag converges to the correct limit as $H/D \rightarrow \infty$. Substituting $Kn = 0.1$ into the theoretical asymptote presented in eqn. (68) and assuming a tangential momentum accommodation coefficient of unity yields:

$$\frac{C_D Re}{12} \rightarrow 1.75 \quad \text{as} \quad H/D \rightarrow \infty \tag{69}$$

Figure 8 confirms that the computed normalised drag coefficients converge to the theoretical asymptote of 1.75, thereby providing an important final validation test. The results in Figure 8 also demonstrate that blockage effects are not as important as the Knudsen number is increased. At the upper limit of the slip flow regime ($Kn = 0.1$), the normalised total drag coefficient for a blockage ratio of $H/D = 2$ is 5.22 whereas the corresponding coefficient in the continuum flow regime (Table 4) is 9.93. This indicates that blockage effects are substantially reduced in the slip flow regime, leading to smaller drag forces on the sphere.

7 Conclusions

An investigation of low Reynolds number rarefied gas flow past a confined microsphere has been conducted using a specially adapted two-dimensional finite-volume Navier-Stokes solver. The hydrodynamic model is applicable to both the continuum and slip flow regimes, and is valid for Knudsen numbers between $0 \le Kn \le 0.1$. In the slip flow regime, rarefaction effects are important but the flow can still be analysed using the Navier-Stokes equations provided appropriate tangential slip-velocity boundary conditions are implemented along the walls of the flow domain.

The present study examines the effects of the Reynolds number and Knudsen number on the drag experienced by a microsphere confined within a circular pipe. In addition, blockage effects are studied by varying the ratio between the diameter of the confining pipe (H) and the diameter of the sphere (D). Model validation has been accomplished by comparing the predicted drag force in the continuum regime against a number of analytical solutions of creeping flow past a confined sphere. The numerical model can also be validated in the slip flow regime by checking that the predicted drag results converge to the theoretical asymptote for an unconfined sphere ($H / D \to \infty$).

At low Reynolds numbers in the continuum flow regime, the results show that the product of the drag coefficient and the Reynolds number collapses to a single coefficient dependent upon the blockage ratio, H / D. The results also indicate that blockage effects are extremely important for continuum flows with very large increases in the drag coefficient being observed for $H / D < 5$. In the slip flow regime, the total drag on the sphere decreases as the Knudsen number is increased, as expected. More importantly, the results suggest that the drag amplification effect caused by blockage ratio becomes less significant as rarefaction starts to influence the flow. This may have important consequences for the design of microfluidic components which operate over a wide range of Knudsen numbers.

References

[1] Gabriel, K., Jarvis, J. & Trimmer, W. (eds.) *Small Machines, Large Opportunities: a report on the emerging field of microdynamics*, National Science Foundation, AT&T Bell Laboratories, Murray Hill, New Jersey, USA, 1988.

[2] Madou, M. *Fundamentals of Microfabrication*, CRC Press, 1997.

[3] Thurigen, C., Beckord, U. & Bessey, R. Construction and manufacturing of a micro gearhead with 1.9mm outer diameter for universal application **in** *Design, Test and Microfabrication of MEMS and MOEMS, Proc. of SPIE*, Vol. 3680, Part 1, pp. 526-533, 1999.

[4] Gravesen, P., Branebjerg, J. & Jensen, O.S. Microfluidics – a review, *J. Micromechanics and Microengineering*, Vol. 3, pp. 168-182, 1993.

[5] Gad-el-Hak, M. The fluid mechanics of microdevices – The Freeman Scholar Lecture, *J. of Fluids Engineering*, Vol. 121, pp. 5-33, 1999.

[6] Weisberg, A., Bau, H.H. & Zemel, J.N. Analysis of microchannels for integrated cooling, *Int. J. Heat & Mass Transfer*, Vol. 35, No. 10, pp. 2465-2474, 1992.

[7] Wegeng, R.S., Call, C.J. & Drost, M.K. Chemical system miniaturisation, Paper no. PNNL-SA-27317, Spring National Meeting of the A.I.Chem.E, New Orleans, 1996

[8] Burns, M.A. *et al*. An integrated nanolitre DNA analysis device, *Science*, Vol. 282, pp. 484-487, 1998.

[9] Kellogg, G.J., Arnold, T.E., Carvalho, B.L., Duffy, D.C. & Sheppard, N.F. Centrifugal microfluidics: applications **in** *Micro Total Analysis Systems 2000, Proc. of the μTAS 2000 Symposium, Enschede, The Netherlands*, pp. 239-242, 2000.

[10] Frye-Mason, G. *et al*. Hand-held miniature chemical analysis system (μChemLab) for detection of trace concentrations of gas phase analytes **in** *Micro Total Analysis Systems 2000, Proc. of the μTAS 2000 Symposium, Enschede, The Netherlands*, pp. 229-232, 2000.

[11] Copley, J. Making waves – fluttering skin could speed up a stealthy sub, *New Scientist*, Vol. 166, Issue 2241, 03/06/2000, p. 15.

[12] Pfahler, J., Harley, J., Bau, H. & Zemel, J.N. Gas and liquid flow in small channels, DSC-Vol. 32, *Micromechanical Sensors, Actuators and Systems*, pp. 49-60, ASME, 1991.

[13] Harley, J.C., Huang, Y., Bau, H.H. & Zemel, J.N. Gas flow in microchannels, *J. Fluid Mech.*, Vol. 284, pp. 257-274, 1995.

[14] Arkilic, E.B. & Breuer, K.S. Gaseous flow in small channels, *AIAA Shear Flow Conference*, Paper no. AIAA 93-3270, Orlando, 1993.

[15] Arkilic, E.B., Breuer, K.S. & Schmidt, M.A. Gaseous flow in microchannels, FED-Vol. 197, *Application of Microfabrication to Fluid Mechanics*, pp. 57-66, ASME, 1994.

[16] Arkilic, E.B., Schmidt, M.A. & Breuer, K.S. Gaseous slip flow in long microchannels, *J. of Micro-Electro-Mechanical Systems*, Vol. 6, No. 2, pp. 167-178, 1997.

[17] Arkilic, E.B. *Measurement of the mass flow and tangential momentum accommodation coefficient in silicon micromachined channels*, Ph.D. Thesis, Massachusetts Institute of Technology, Cambridge, Massachusetts, 1997.
[18] *CRC Handbook of Chemistry and Physics*, 80th Ed., CRC Press, 1999-2000.
[19] Schaaf, S.A. & Chambre, P.L. *Flow of Rarefied Gases*, Princeton University Press, 1961.
[20] Bird, G.A. *Molecular Gas Dynamics and the Direct Simulation of Gas Flows*, Clarendon Press, Oxford, 1994.
[21] Fremerey, J.K. Spinning rotor vacuum gauges, *Vacuum*, Vol. 32, pp. 685-690, 1982.
[22] Fremerey, J.K. The spinning rotor gauge, *J. Vacuum Science and Technology A*, Vol. 3(3), pp. 1715-1720, 1985.
[23] Reich, G. Spinning rotor viscosity gauge: A transfer standard for the laboratory or an accurate gauge for vacuum process control, *J. Vacuum Science and Technology*, Vol. 20(4), pp. 1148-1152, 1982.
[24] Shastry, M.C.R., Luck, S.D. & Roder, H. A continuous-flow capillary mixing method to monitor reactions on the microsecond time scale, *Biophysical Journal*, Vol. 74, pp. 2714-2721, 1998.
[25] Liu, H-C. F., Beskok, A., Gatsonis, N. & Karniadakis, G.E. Flow past a micro-sphere in a pipe: effects of rarefaction, DSC-Vol. 66, *Micro-Electro-Mechanical Systems (MEMS)*, pp. 445-452, ASME, 1998.
[26] Wakiya, S. A spherical obstacle in the flow of a viscous fluid through a tube, *J. Phys. Soc. Japan*, Vol. 8, No. 2, pp. 254-257, 1953.
[27] Wakiya, S. Viscous flows past a spheroid, *J. Phys. Soc. Japan*, Vol. 12, No. 10, pp. 1130-1141, 1957.
[28] Bohlin, T. *Trans. Roy. Inst. Technology* (Stockholm), No. 155, 1960.
[29] Haberman, W.L. & Sayre, R.M. *David Taylor Model Basin Report No. 1143*, Washington, D.C., U.S. Navy Dept., 1958.
[30] Happel, J. & Brenner, H. *Low Reynolds Number Hydrodynamics*, Martinus Nijhoff Publishers, Dordrecht, 1986.
[31] Stokes, G.G. On the theories of internal friction of fluids in motion, *Trans. Cambridge Philosophical Society*, Vol. 8, pp. 287-305, 1845.
[32] Gad-el-Hak, M. Questions in Fluid Mechanics: Stokes' hypothesis for a Newtonian, isotropic fluid, *J. of Fluids Engineering*, Vol. 117, pp. 3-5, 1995.
[33] Basset, A.B. *A Treatise on Hydrodynamics*, Cambridge University Press, 1888.
[34] Arkilic, E.B., Schmidt, M.A. & Breuer, K.S. TMAC measurement in silicon micromachined channels, *Rarefied Gas Dynamics 20*, Beijing University Press, 1997.
[35] Gu, X.J. & Emerson, D.R. *THOR-2D: A two-dimensional computational fluid dynamics code*, Technical Report, Department of Computational Science and Engineering, CLRC Daresbury Laboratory, June 2000.
[36] Barber, R.W. & Emerson, D.R. *A numerical study of low Reynolds number slip flow in the hydrodynamic development region of circular and parallel plate ducts*, Technical Report DL-TR-00-002, Department of Computational Science and Engineering, CLRC Daresbury Laboratory, December 2000.
[37] Schlichting, H. *Boundary-Layer Theory*, 3rd English Ed., McGraw-Hill, 1968.

[38] Press, W.H., Teukolsky, S.A., Vetterling, W.T. & Flannery, B.P. *Numerical Recipes in Fortran: The Art of Scientific Computing*, 2nd Ed., Cambridge University Press, 1992.
[39] Richardson, S.M. *Fluid Mechanics*, Hemisphere Publishing Corp., 1989.
[40] Stokes, G.G. On the effect of the internal friction of fluids on the motion of pendulums, *Cambridge Phil. Trans.*, Vol. 9, pp. 8-106, 1851.
[41] Shah, R.K. & London, A.L. *Laminar Flow Forced Convection in Ducts*, Academic Press, New York, 1978.
[42] Faxen, H. Die Bewegung einer starren Kugel längs der Achse eines mit zäher Flüssigkeit gefüllten Rohres, *Arkiv. Mat. Astron. Fys.*, **17**, No. 27, pp. 1-28, 1923.
[43] Barber, R.W. & Emerson, D.R. *Analytical solution of low Reynolds number slip flow past a sphere*, Technical Report DL-TR-00-001, Department of Computational Science and Engineering, CLRC Daresbury Laboratory, December 2000.
[44] Goldberg, R. *The slow flow of a rarefied gas past a spherical obstacle*, Ph.D. Thesis, New York Univ., 1954.
[45] Beskok, A. & Karniadakis, G.E. Simulation of heat and momentum transfer in complex microgeometries, *J. Thermophysics and Heat Transfer*, Vol. 8, No. 4, pp. 647-655, 1994.
[46] Lien, F-S. *Computational modelling of 3D flow in complex ducts and passages*, Ph.D. Thesis, University of Manchester Institute of Science and Technology, 1992.

Appendix A

Determination of the mean free path of a gas

For an ideal gas modelled as rigid spheres of collision diameter, σ_c, the mean distance travelled by a molecule between successive collisions or *mean free path*, $\mathcal{L}$, is given by [18]:

$$\mathcal{L} = \frac{kT}{\sqrt{2}\,\pi\, p\, \sigma_c^2} \tag{1}$$

where,

k = Boltzmann's constant = 1.380662×10^{-23} J / K,

T = temperature (K),

p = pressure (N/m^2) and

σ_c = collision diameter of the molecules (m).

At standard ambient temperature and pressure (SATP), defined as T = 298.15 K and $p = 10^5$ N/m^2, eqn. (1) becomes:

$$\mathcal{L} = \frac{9.265\times10^{-27}}{\sigma_c^{\,2}} \tag{2}$$

For air, the average collision diameter of the molecules is 3.66×10^{-10} m giving a mean free path of 6.92×10^{-8} m (or 69.2 nm). The collision diameters of other common gases are listed below:

Gas	σ_c (m)
Air	3.66×10^{-10}
Ar	3.58×10^{-10}
CO_2	4.53×10^{-10}
H_2	2.71×10^{-10}
He	2.15×10^{-10}
Kr	4.08×10^{-10}
N_2	3.70×10^{-10}
NH_3	4.32×10^{-10}
Ne	2.54×10^{-10}
O_2	3.55×10^{-10}
Xe	4.78×10^{-10}

Table A1: Collision diameters of common gases [18]

Appendix B

Generalised stress tensor transformation procedure

The governing hydrodynamic equations are solved using THOR-2D, a two-dimensional finite-volume Navier-Stokes solver developed by the Computational Engineering Group at CLRC Daresbury Laboratory (Gu & Emerson [35]). In order to extend the solver to the slip-flow regime ($0 < Kn \leq 0.1$), additional subroutines have been developed to account for the tangential slip-velocity boundary condition at the walls of the flow domain. In particular, the slip-velocity constraint requires the tangential shear stress to be calculated at every grid node along a solid-fluid interface. Since the governing hydrodynamic equations are solved using a non-orthogonal boundary-fitted co-ordinate system, the tangential shear stress has to be calculated using a generalised stress tensor transformation procedure to account for the non-orthogonality of the grid lines. Furthermore, the determination of the drag force on the microsphere requires both the tangential shear stress component and the normal stress component to be computed around the perimeter. It is therefore necessary to transform the axisymmetric (x, r) co-ordinate stress tensor into a localised co-ordinate reference frame based upon the orientation of the boundary surface.

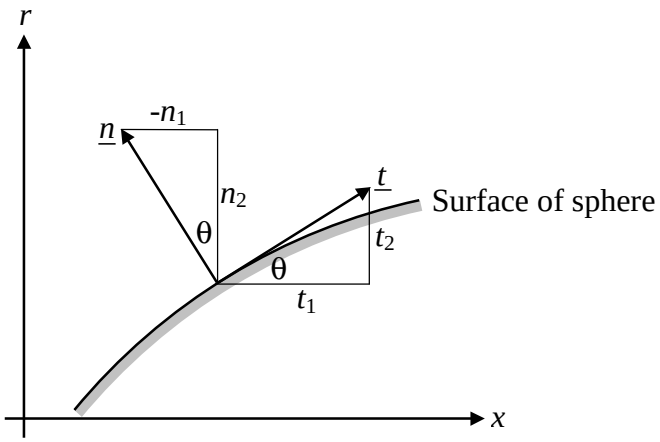

Figure B1: Definition sketch of normal and tangential base vectors

Consider an arbitrary section along the boundary of the sphere as shown in Figure B1. Let $\underline{n}$ and $\underline{t}$ denote the local unit normal and tangential vectors of the surface as shown above:

$$\underline{n} = n_1 \underline{i} + n_2 \underline{j} \quad \text{and} \quad \underline{t} = t_1 \underline{i} + t_2 \underline{j} \tag{1}$$

It can be seen that the coefficients in eqn. (1) are related via

$$t_1 = n_2 \quad \text{and} \quad t_2 = -n_1 \tag{2}$$

In the (x, r) plane, the stress tensor for an incompressible flow is given by

$$[\tau]=\begin{bmatrix}\tau_{11} & \tau_{12}\\ \tau_{21} & \tau_{22}\end{bmatrix}=\begin{bmatrix}2\mu\frac{\partial u}{\partial x} & \mu\left(\frac{\partial u}{\partial r}+\frac{\partial v}{\partial x}\right)\\ \mu\left(\frac{\partial v}{\partial x}+\frac{\partial u}{\partial r}\right) & 2\mu\frac{\partial v}{\partial r}\end{bmatrix} \tag{3}$$

The problem is therefore to transform $[\tau]$ into a generalised stress tensor $[\tau']$ related to the normal and tangential base vectors, $\underline{n}$ and $\underline{t}$. Lien [46] has demonstrated that in the transformed domain, the stress tensor can be expressed as

$$[\tau']=[G][\tau][G]^{\mathrm{T}} \tag{4}$$

where the matrix $[G]$ is given by

$$[G]=\begin{bmatrix}t_1 & t_2\\ n_1 & n_2\end{bmatrix} \tag{5}$$

and the superscript$^{\mathrm{T}}$ denotes the transpose of a matrix. Consequently, the generalised stress tensor can be evaluated as

$$[\tau']=\begin{bmatrix}\tau'_{11} & \tau'_{12}\\ \tau'_{21} & \tau'_{22}\end{bmatrix}=\begin{bmatrix}t_1 & t_2\\ n_1 & n_2\end{bmatrix}\begin{bmatrix}\tau_{11} & \tau_{12}\\ \tau_{21} & \tau_{22}\end{bmatrix}\begin{bmatrix}t_1 & n_1\\ t_2 & n_2\end{bmatrix} \tag{6}$$

which yields after multiplication (and simplification using $\tau_{21}=\tau_{12}$):

$$\begin{bmatrix}\tau'_{11} & \tau'_{12}\\ \tau'_{21} & \tau'_{22}\end{bmatrix}=\begin{bmatrix}t_1^2\tau_{11}+2t_1t_2\,\tau_{12}+t_2^2\tau_{22} & t_1n_1\tau_{11}+(t_1n_2+t_2n_1)\,\tau_{12}+t_2n_2\tau_{22}\\ t_1n_1\tau_{11}+(t_1n_2+t_2n_1)\,\tau_{12}+t_2n_2\tau_{22} & n_1^2\tau_{11}+2n_1n_2\,\tau_{12}+n_2^2\tau_{22}\end{bmatrix} \tag{7}$$

Hence, the tangential shear stress on the surface of the sphere is given by

$$\tau'_{12}=t_1n_1\tau_{11}+(t_1n_2+t_2n_1)\,\tau_{12}+t_2n_2\tau_{22} \tag{8}$$

whilst the normal stress is given by

$$\tau'_{22}=n_1^2\tau_{11}+2n_1n_2\,\tau_{12}+n_2^2\tau_{22} \tag{9}$$

The tangential shear stress is then used to evaluate the slip-velocity along the wall of the microsphere. Specifically, the tangential slip-velocity u_t is found using eqn. (16) of Section 3:

$$u_t=\frac{2-\sigma}{\sigma}\frac{Kn\,D}{\mu}\tau'_{12} \tag{10}$$

Substituting for the tangential shear stress from eqn (8) yields

$$u_t=\frac{2-\sigma}{\sigma}\frac{Kn\,D}{\mu}\left(\,t_1n_1\tau_{11}+(t_1n_2+t_2n_1)\,\tau_{12}+t_2n_2\tau_{22}\,\right) \tag{11}$$

A similar technique is implemented at the pipe wall.

Blockage ratio H / D	Computational domain[+]	Mesh resolution
2.0	$-10a \le x \le 10a$	140×25
2.5	$-10a \le x \le 10a$	140×35
3.0	$-10a \le x \le 10a$	140×35
3.5	$-10a \le x \le 10a$	140×35
4.0	$-10a \le x \le 10a$	140×50
4.5	$-10a \le x \le 10a$	140×50
5.0	$-10a \le x \le 10a$	140×60
7.5	$-15a \le x \le 15a$	140×80
10.0	$-15a \le x \le 15a$	140×100
20.0	$-25a \le x \le 25a$	140×100
40.0	$-50a \le x \le 50a$	140×100

[+] Minimum length of flow domain chosen as $-10a \le x \le 10a$ for compatibility with Liu *et al*. [25]

Table 1: Computational meshes employed in blockage ratio study

Re	Normalised drag coefficients, $C_D Re/12$		
	Skin-friction drag	Pressure drag	Total drag
0.500	4.793	5.140	9.933
0.250	4.792	5.139	9.931
0.125	4.792	5.139	9.931
0.050	4.792	5.139	9.931
0.010	4.792	5.139	9.931

Table 2: Normalised drag coefficients in the continuum flow regime as a function of Reynolds number for a blockage ratio of $H/D = 2$

Re	Normalised drag coefficients, $C_D Re/12$		
	Skin-friction drag	Pressure drag	Total drag
0.500	1.680	0.881	2.561
0.250	1.652	0.866	2.518
0.125	1.635	0.856	2.491
0.050	1.629	0.853	2.482
0.010	1.628	0.852	2.480

Table 3: Normalised drag coefficients in the continuum flow regime as a function of Reynolds number for a blockage ratio of $H/D = 10$

Blockage ratio H / D	Normalised drag coefficients, $C_D Re/12$		
	Skin-friction drag	Pressure drag	Total drag
2.0	4.792	5.139	9.931
2.5	3.488	2.918	6.406
3.0	2.879	2.094	4.973
3.5	2.529	1.687	4.216
4.0	2.317	1.446	3.763
4.5	2.163	1.294	3.457
5.0	2.051	1.190	3.241
7.5	1.778	0.964	2.742
10.0	1.635	0.856	2.491
20.0	1.478	0.753	2.231
40.0	1.357	0.688	2.045

Table 4: Normalised drag coefficients in the continuum flow regime as a function of blockage ratio for a fully-developed entrance velocity profile ($Re = 0.125$)

Blockage ratio H / D	Normalised drag coefficients, $C_D Re/12$		
	Skin-friction drag	Pressure drag	Total drag
2.0	4.774	5.120	9.894
2.5	3.480	2.911	6.391
3.0	2.873	2.090	4.963
3.5	2.524	1.684	4.208
4.0	2.314	1.444	3.758
4.5	2.159	1.292	3.451
5.0	2.049	1.189	3.238
7.5	1.773	0.962	2.735
10.0	1.631	0.854	2.485
20.0	1.468	0.746	2.214
40.0	1.354	0.685	2.039

Table 5: Normalised drag coefficients in the continuum flow regime as a function of blockage ratio for a uniform entrance velocity profile ($Re = 0.125$)

Length of computational domain	Normalised drag coefficients, $C_D Re/12$		
	Skin-friction drag	Pressure drag	Total drag
$-50a \le x \le 50a$	1.354	0.685	2.039
$-20a \le x \le 20a$	1.072	0.542	1.614
$-15a \le x \le 15a$	0.857	0.433	1.290
$-10a \le x \le 10a$	0.747	0.377	1.124

Table 6: Normalised drag coefficients in the continuum flow regime as a function of entrance location for a blockage ratio of $H/D = 40$ ($Re = 0.125$)

Kn	Normalised drag coefficients, $C_D Re/12$			
	Skin-friction drag	Normal stress drag	Pressure drag	Total drag
0	4.792	$(0.076)^+$	5.139	10.007
0.02	3.646	0.354	4.240	8.240
0.04	2.921	0.520	3.649	7.090
0.06	2.424	0.628	3.230	6.282
0.08	2.064	0.702	2.916	5.682
0.10	1.792	0.754	2.671	5.217

$^+$ Normal stress drag is theoretically zero for $Kn \to 0$

Table 7: Normalised drag coefficients as a function of Knudsen number for a blockage ratio of $H/D = 2$ ($Re = 0.125$)

Kn	Normalised drag coefficients, $C_D Re/12$			
	Skin-friction drag	Normal stress drag	Pressure drag	Total drag
0	2.051	$(0.048)^+$	1.190	3.289
0.02	1.759	0.182	1.106	3.047
0.04	1.535	0.283	1.038	2.856
0.06	1.358	0.360	0.983	2.701
0.08	1.215	0.420	0.937	2.572
0.10	1.097	0.467	0.898	2.462

$^+$ Normal stress drag is theoretically zero for $Kn \to 0$

Table 8: Normalised drag coefficients as a function of Knudsen number for a blockage ratio of $H/D = 5$ ($Re = 0.125$)

Kn	Normalised drag coefficients, $C_D Re/12$			
	Skin-friction drag	Normal stress drag	Pressure drag	Total drag
0	1.357	$(0.038)^+$	0.688	2.083
0.02	1.207	0.130	0.660	1.997
0.04	1.087	0.205	0.638	1.930
0.06	0.988	0.265	0.619	1.872
0.08	0.905	0.316	0.603	1.824
0.10	0.835	0.358	0.590	1.783

$^+$ Normal stress drag is theoretically zero for $Kn \to 0$

Table 9: Normalised drag coefficients as a function of Knudsen number for a blockage ratio of $H/D = 40$ ($Re = 0.125$)

Blockage ratio H / D	Normalised drag coefficients, $C_D Re/12$			
	Skin-friction drag	Normal stress drag	Pressure drag	Total drag
2.0	1.792	0.754	2.671	5.217
2.5	1.498	0.625	1.765	3.888
3.0	1.341	0.569	1.376	3.286
3.5	1.242	0.537	1.167	2.946
4.0	1.181	0.502	1.042	2.725
4.5	1.134	0.483	0.964	2.581
5.0	1.097	0.467	0.898	2.462
7.5	0.979	0.419	0.753	2.151
10.0	0.953	0.407	0.699	2.059
20.0	0.896	0.383	0.632	1.911
40.0	0.835	0.358	0.590	1.783

Table 10: Normalised drag coefficients in the slip flow regime as a function of blockage ratio ($Re = 0.125$, $Kn = 0.1$)

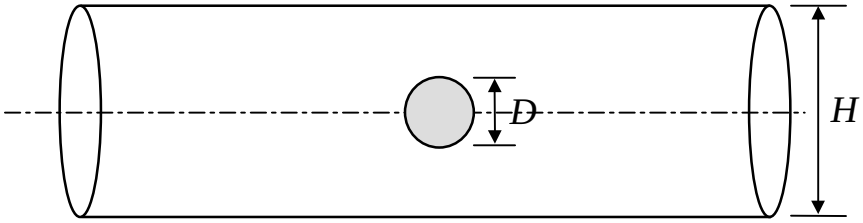

Figure 1: Problem formulation:- a confined sphere inside a circular pipe

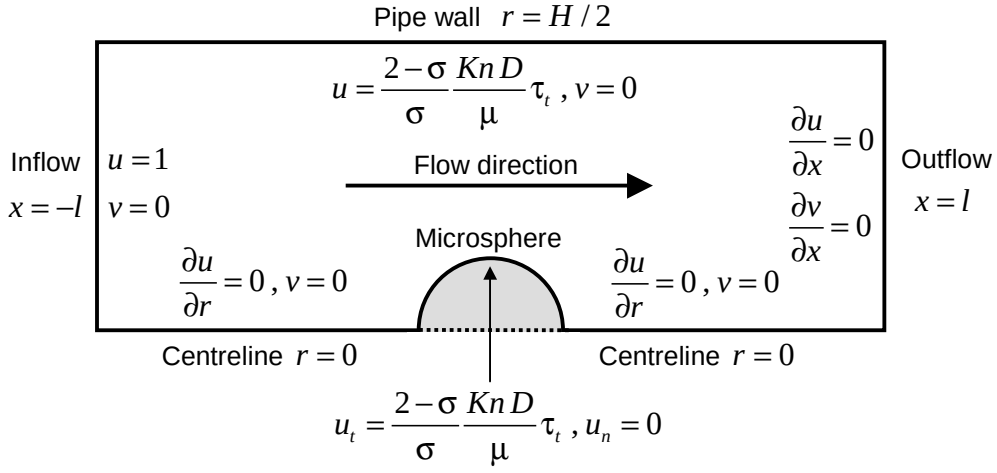

Figure 2: Schematic diagram of boundary conditions for confined microsphere geometry

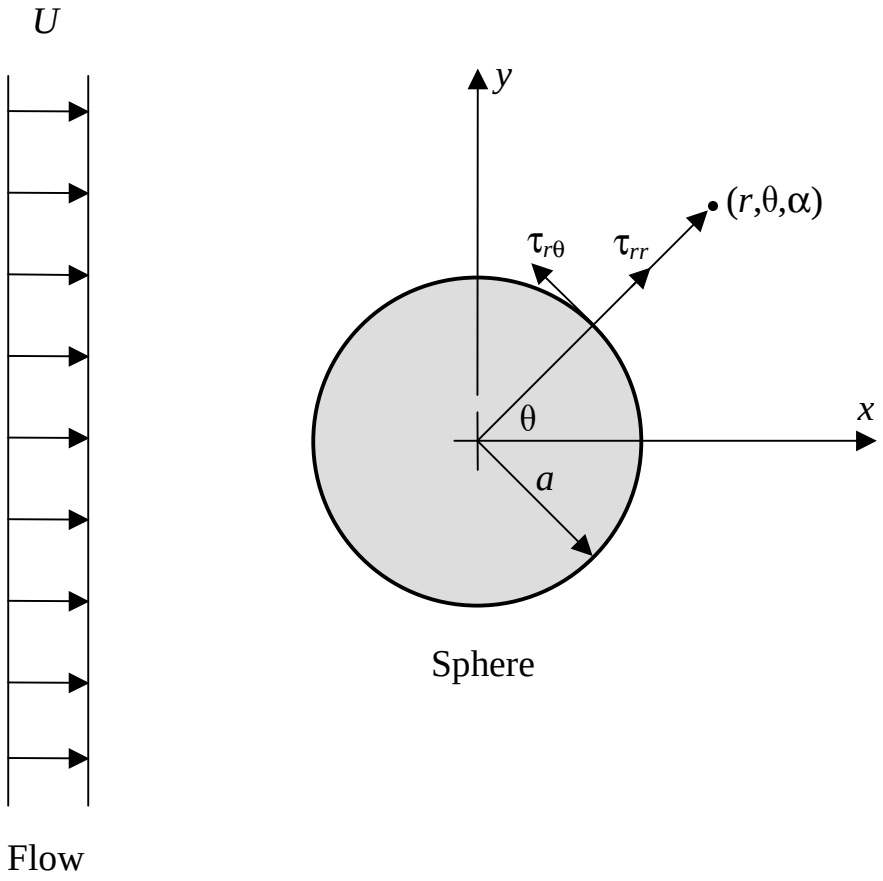

Figure 3: Localised spherical polar co-ordinate reference frame (r, θ, α) and shear stresses around microsphere

(a) Blockage ratio $H / D = 2$

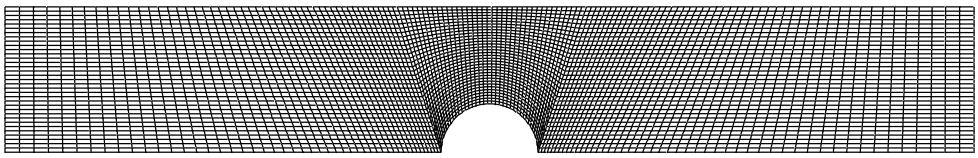

(b) Blockage ratio $H / D = 3$

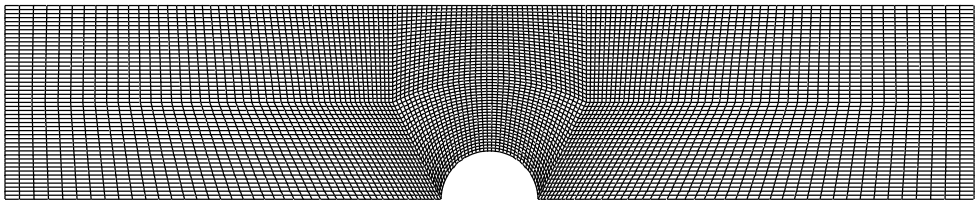

(c) Blockage ratio $H / D = 4$

Figure 4: Axisymmetric flow domains for a confined sphere in a circular pipe

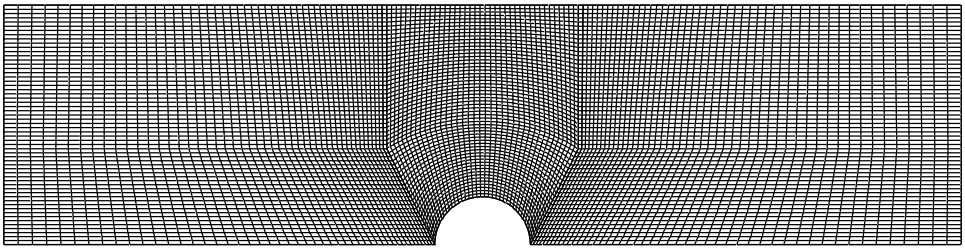

(d) Blockage ratio $H / D = 5$

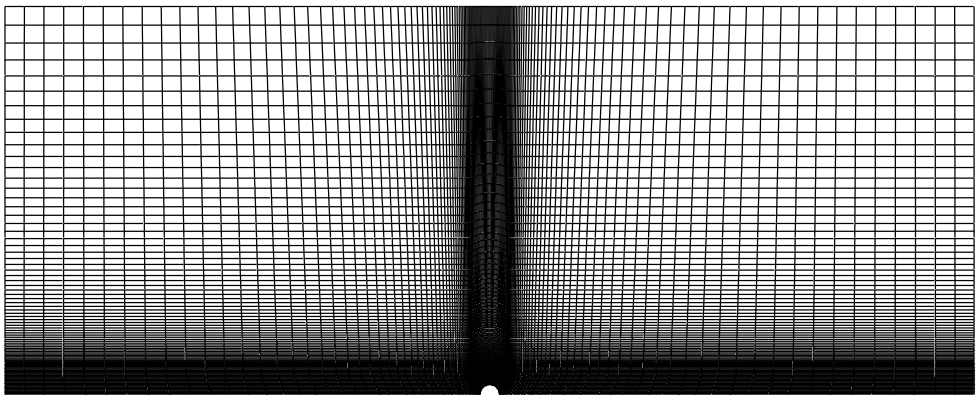

(e) Blockage ratio $H / D = 40$

Figure 4: Axisymmetric flow domains for a confined sphere in a circular pipe

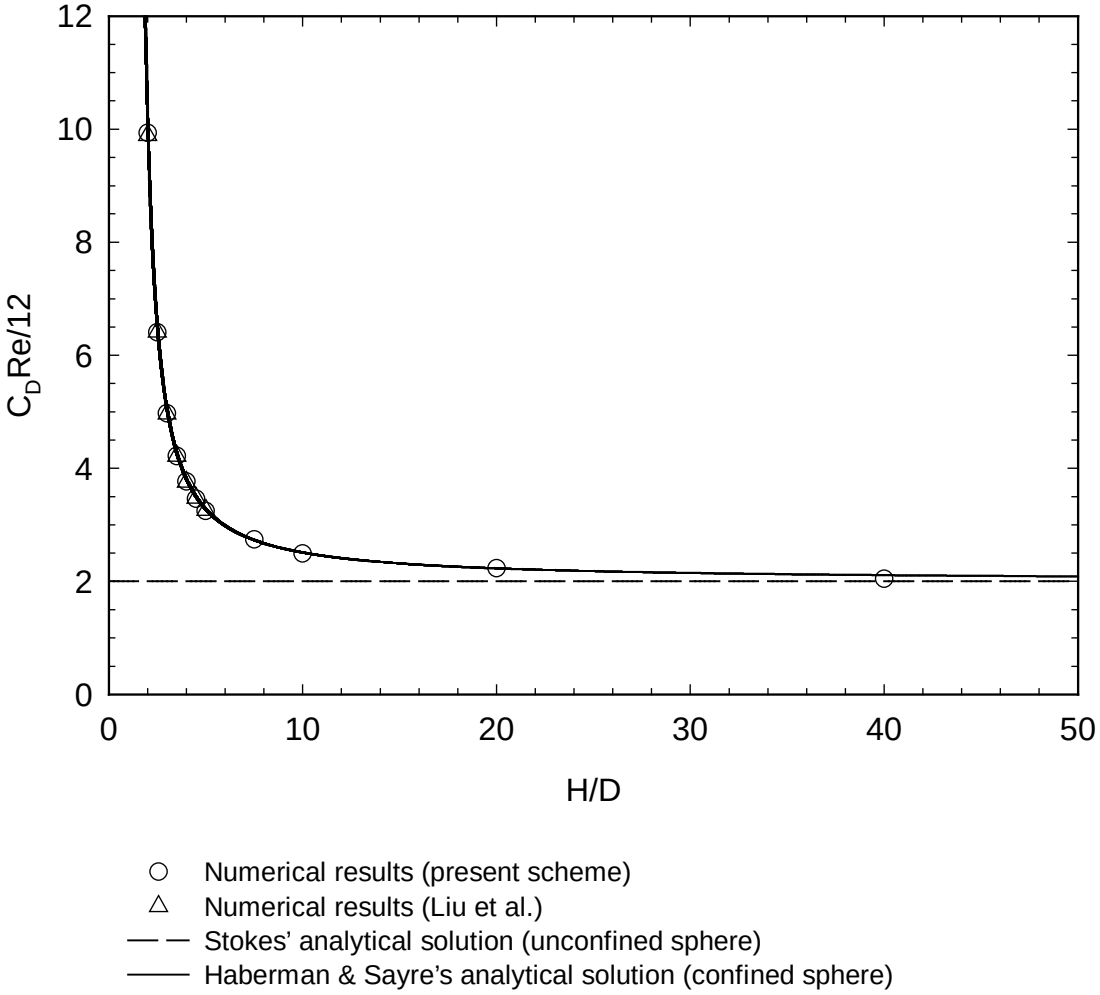

Figure 5: Variation of normalised total drag coefficient in the continuum flow regime as a function of blockage ratio ($Re = 0.125$)

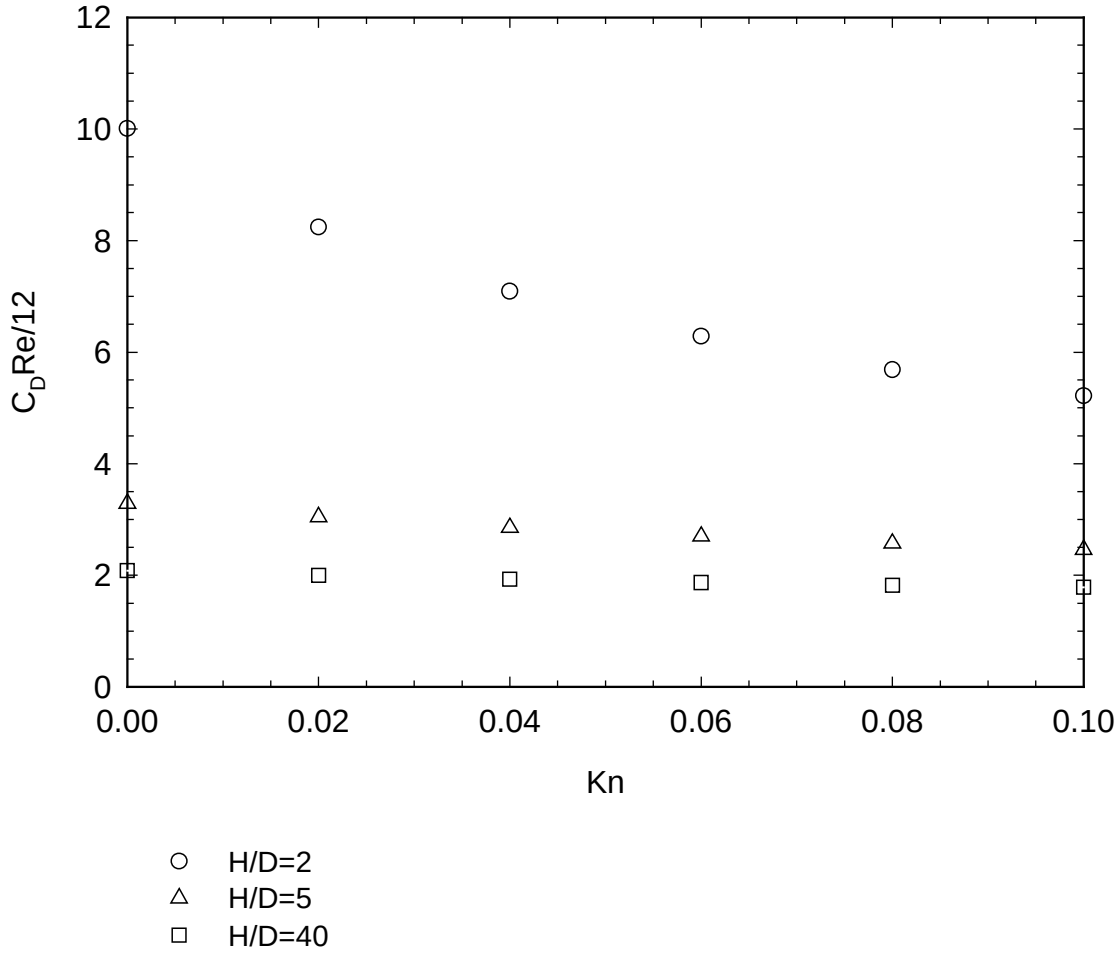

Figure 6: Variation of normalised total drag coefficient in the slip flow regime as a function of Knudsen number ($Re = 0.125$)

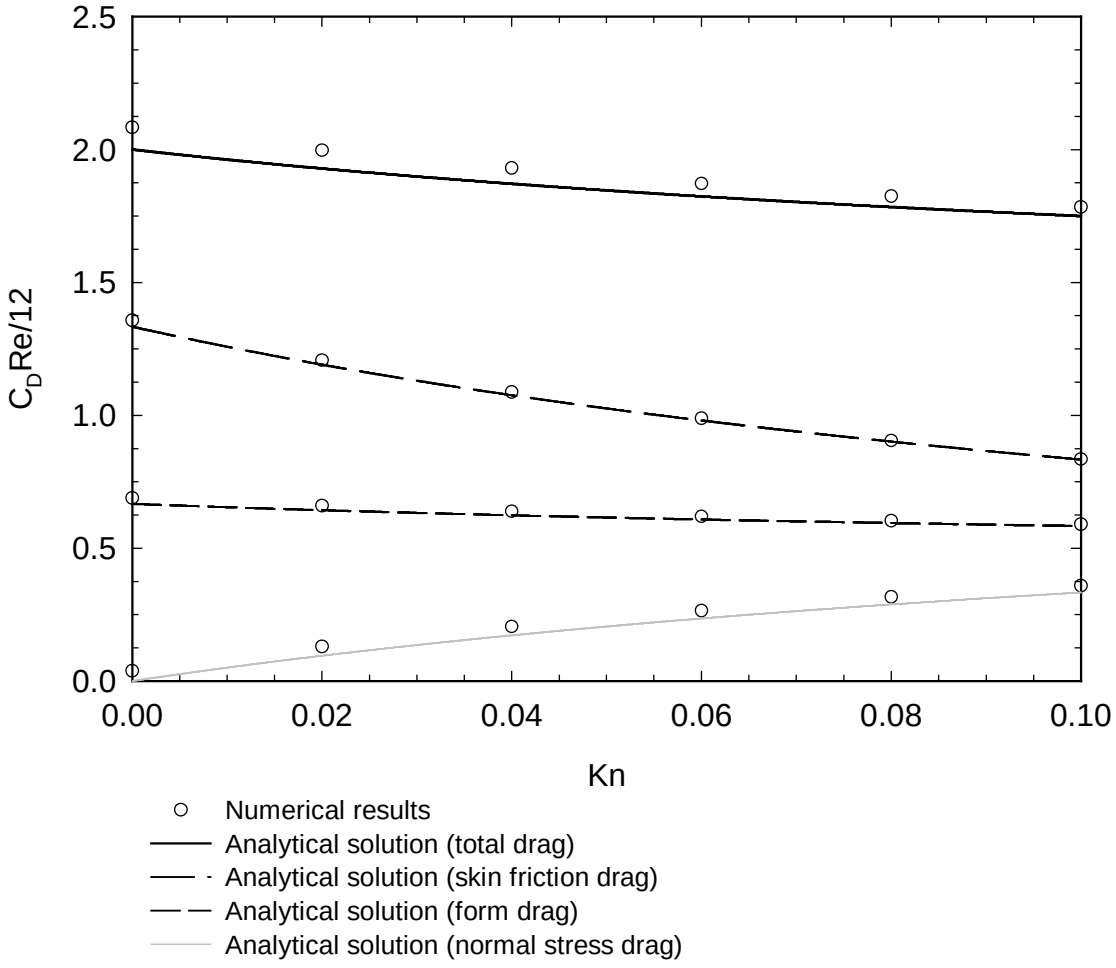

Figure 7: Variation of normalised drag coefficients as a function of Knudsen number for a blockage ratio of $H/D = 40$ ($Re = 0.125$)

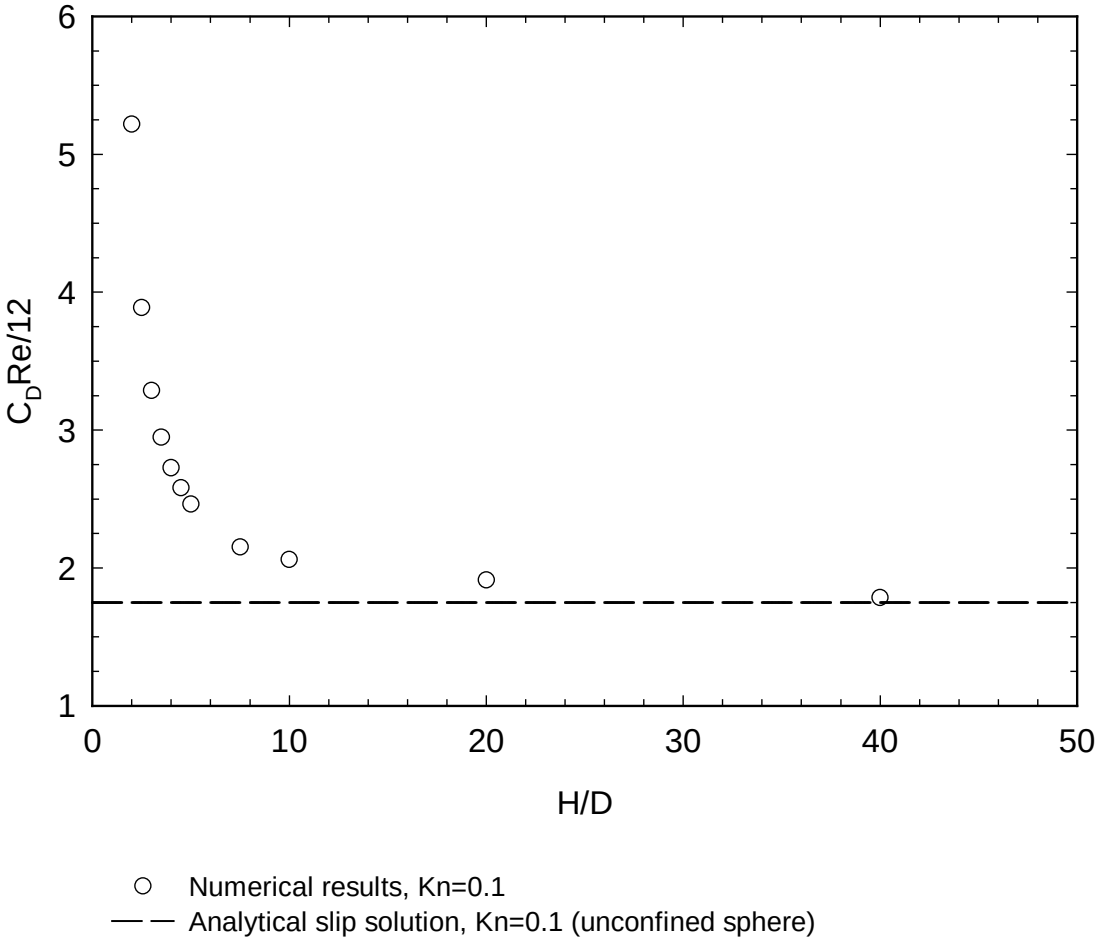

Figure 8: Variation of normalised total drag coefficient in the slip flow regime as a function of blockage ratio ($Re = 0.125$, $Kn = 0.1$)